Thickness dependence of the mechanical properties of piezoelectric high-Q<inf>m</inf> nanomechanical resonators made from aluminium

Downloaded from: https://research.chalmers.se, 2025-01-15 16:01 UTC

Citation for the original published paper (version of record):
Ciers, A., Jung, A., Ciers, J. et al (2024). Thickness dependence of the mechanical properties of piezoelectric high-Q<inf>m</inf>
nanomechanical resonators made from aluminium nitride. Materials for Quantum Technology, 4(4).
http://dx.doi.org/10.1088/2633-4356/ad9b64

N.B. When citing this work, cite the original published paper.

research.chalmers.se offers the possibility of retrieving research publications produced at Chalmers University of Technology. It covers all kind of research output: articles, dissertations, conference papers, reports etc. since 2004. research.chalmers.se is administrated and maintained by Chalmers Library

(article starts on next page)

Materials for Quantum Technology

PAPER • OPEN ACCESS

Thickness dependence of the mechanical properties of piezoelectric high-Q_m nanomechanical resonators made from aluminium nitride

To cite this article: Anastasiia Ciers *et al* 2024 *Mater. Quantum. Technol.* **4** 046301

View the article online for updates and enhancements.

You may also like

- Spin-active defects in hexagonal boron nitride
  Wei Liu, Nai-Jie Guo, Shang Yu et al.
- Fiber-coupled quantum light sources based on solid-state quantum emitters
  Lucas Bremer, Sven Rodt and Stephan Reitzenstein
- Anti-Stokes excitation of optically active point defects in semiconductor materials
  Wu-Xi Lin, Jun-Feng Wang, Qiang Li et al.

This content was downloaded from IP address 129.16.140.115 on 10/01/2025 at 10:06

IOP Publishing Mater. Quantum Technol. 4 (2024) 046301 https://doi.org/10.1088/2633-4356/ad9b64

Materials for Quantum Technology

OPEN ACCESS

RECEIVED
4 October 2024

REVISED
14 November 2024

ACCEPTED FOR PUBLICATION
6 December 2024

PUBLISHED
30 December 2024

Original Content from this work may be used under the terms of the Creative Commons Attribution 4.0 licence.

Any further distribution of this work must maintain attribution to the author(s) and the title of the work, journal citation and DOI.

PAPER

Thickness dependence of the mechanical properties of piezoelectric high-Q_m nanomechanical resonators made from aluminium nitride

Anastasiia Ciers[1,*], Alexander Jung[1], Joachim Ciers[1], Laurentius Radit Nindito[1], Hannes Pfeifer[1], Armin Dadgar[2], Jürgen Bläsing[2], André Strittmatter[2] and Witlef Wieczorek[1,*]

[1] Department of Microtechnology and Nanoscience (MC2), Chalmers University of Technology, SE-412 96 Gothenburg, Sweden
[2] Institute of Physics, Otto-von-Guericke-University Magdeburg, DE-39106 Magdeburg, Germany
[*] Authors to whom any correspondence should be addressed.

E-mail: anastasiia.ciers@chalmers.se and witlef.wieczorek@chalmers.se

Keywords: nanomechanics, sensing, nanotechnology, appled physics, quantum technology

Abstract

Nanomechanical resonators with high quality factors (Q_m) enable mechanics-based quantum technologies, in particular quantum sensing and quantum transduction. High-Q_m nanomechanical resonators in the kHz to MHz frequency range can be realized in tensile-strained thin films that allow the use of dissipation dilution techniques to drastically increase Q_m. In our work, we study the material properties of tensile-strained piezoelectric films made from aluminium nitride (AlN). We characterize crystalline AlN films with a thickness ranging from 45 nm to 295 nm, which are directly grown on Si(111) by metal–organic vapour-phase epitaxy. We report on the crystal quality and surface roughness, the piezoelectric response, and the residual and released stress of the AlN thin films. Importantly, we determine the intrinsic quality factor of the films at room temperature in high vacuum. We fabricate and characterize AlN nanomechanical resonators that exploit dissipation dilution to enhance the intrinsic quality factor by utilizing the tensile strain in the film. We find that AlN nanomechanical resonators below 200 nm thickness exhibit the highest $Q_m \times f_m$-product, on the order of 10^{12} Hz. We discuss possible strategies to optimize the material growth that should lead to devices that reach even higher $Q_m \times f_m$-products. This will pave the way for future advancements of optoelectromechanical quantum devices made from tensile-strained piezoelectric AlN.

1. Introduction

Nanoelectromechanical systems [1] are utilized in a broad range of sensing applications, including the detection of mass [2], force [3], or spin [4]. These applications are enabled by the high resonance frequency, small mass, or large mechanical quality factor of nanoelectromechanical systems. Recently, nano- and micromechanical systems have found their way into quantum technologies [5, 6], particularly as quantum sensors or quantum transducers. A crucial factor in these advancements was the engineering of ultra-high quality factors in these systems [7]. Nowadays quality factors of up to 10^{10} can be achieved with strained Si [8] or SiN [9] nanomechanical resonators, with Si optomechanical crystals at ultra-low temperature [10], or with trapped SiO_2 nanospheres [11].

Dissipation dilution techniques are employed to realize chip-based mechanical resonators with ultra-high mechanical quality factors in the kHz to MHz frequency range [7, 12–14]. Essentially, mechanical dissipation is reduced in tensile-strained films with a large aspect ratio by storing mechanical energy as lossless tension energy rather than as lossy bending energy [14]. The increase in quality factor is quantified by the dilution factor, which dilutes the material-dependent intrinsic quality factor.

Dissipation dilution techniques have been applied to amorphous as well as crystalline materials. The latter could offer larger intrinsic quality factors due to a lower defect density. A major advantage of crystalline

© 2024 The Author(s). Published by IOP Publishing Ltd

materials is the possibility for in-built functionality, which can be used, for example, for read-out or actuation of mechanical motion. In particular, piezoelectric films offer the possibility to directly couple mechanical with electrical degrees of freedom, and when also interfacing to light, hybrid optoelectromechanical quantum devices can be realized [15]. Tensile-strained piezoelectric materials that have been used so far to realize high-Q_m nanomechanical resonators were InGaP [16–18], SiC [19, 20], and aluminium nitride (AlN) [21]. AlN is widely used in classical technologies, for example, in telecommunication due to its high acoustic velocity, piezoelectricity [22], low dielectric loss, and mechanical strength [23]. Applications include multi-frequency bandpass filters, parametric feedback oscillators, and gas sensors [24–26]. In quantum technologies, non-strained AlN resonators operating at GHz frequencies have for example been coupled to superconducting qubits [27]. We have recently demonstrated that a highly-tensile strained 295 nm-thick AlN film can be used to realize nanomechancial resonators with a Q_m exceeding 10^7 [21], opening the possibility to realize AlN-based high-Q_m optoelectromechanical quantum devices.

The present work systematically studies the material properties of tensile-strained AlN thin films for realizing high-Q_m nanomechanical resonators. We study AlN thin films with a thickness between 45 nm to 295 nm that are epitaxially grown on (111)-oriented Si wafers by metal–organic vapour-phase epitaxy (MOVPE). Our study is motivated by the fact that the dilution factor is expected to increase for thinner films. This would result in an increase of Q_m [14] provided that the film's residual strain and intrinsic quality factor is not reduced. We characterize the crystal structure quality of the AlN films, their surface roughness, and evaluate the residual stress of the thin films. We then fabricate AlN cantilevers to determine the Young's modulus of the AlN films. We find that the released cantilevers exhibit bending, indicating inhomogeneous strain within the film. This motivates us to introduce a simple bilayer model, which we further use in finite element method (FEM) simulations of various nanomechanical resonator geometries. Importantly, we determine the intrinsic quality factor and released stress of each AlN film. Finally, we fabricate a high-Q_m triangline-shaped nanomechanical resonator in the 90 nm-thick AlN film, the thinnest AlN film that withstands the release step of the fabrication process. This triangline resonator exhibits a $Q_m \times f_m$-product for its fundamental mode of 3.7×10^{12} Hz, a factor of two larger than what would be expected from a similar triangline in 295 nm-thick AlN.

2. Material characterization

2.1. Crystal structure

Silicon substrates used for the epitaxial growth of III-nitrides (InN, GaN, AlN and their alloys) offer significant technological advantages over other growth substrates such as scalability and the ability to integrate III-nitride devices with silicon microelectronics on a single wafer. We grow our AlN film by MOVPE on 2 inch (111)-oriented 500 μm-thick Si wafers (for details see appendix A.1). The resulting wurtzite AlN (see figure 1(a)) has a polar axis along the [0001] direction, i.e. the c-axis [21].

The bond lengths of AlN and Si differ by 16.7%, which leads to a lattice mismatch and a high defect density in the lower 70 nm region of the AlN film. III-nitrides grown on a Si substrate host all major defect types: point defects, line defects, plane defects and inversion domains [28].

The crystallinity and dislocation density of the AlN film were analyzed by high resolution x-ray diffraction (HRXRD), details see appendix A.2. To this end the detector angle is fixed and the incident x-ray beam angle is scanned (ω-scan) around the (0002) or the $(10\bar{1}0)$ plane. A narrower full width at half maximum (FWHM) of the observed diffraction peak corresponds to less disorder of the crystal plane. We evaluate the c-axis disorder using the ω-scan of the AlN (0002) peak, while the twist distribution around the c-axis is evaluated via the $(10\bar{1}0)$ peak, as shown in figure 1(b).

The AlN quality clearly improves with increasing thickness [29], as the FWHM of the corresponding peaks decreases with an increase in film thickness. Figure 1(c) shows the lattice constants a and c, which are calculated from the HRXRD $2\Theta/\theta$ data using the Bragg law and interplanar spacing formula [30]. The observed lattice constant evolution with AlN thickness can be explained as follows. Initially, there is a high density of small low-strain AlN crystallites. With increasing film thickness these crystallites coalesce and the film quality improves due to a reduction in grain boundaries and dislocations. This is accompanied by an increased stress in the film [31]. Thus, the lattice constants are deviating stronger from the single-crystal values for thicker AlN films.

As the AlN film on the Si substrate is grown at high temperatures (above 900 °C, see appendix A.1) after cooldown a large tensile stress is generated due to the thermal expansion mismatch between Si and AlN [32]. The resulting biaxial tension could be partially relaxed if the crystal structure would posses a plane along which the dislocations can move. For wurtzite III-nitride materials the primary slip plane is (0001). However, breaking the covalent Al-N bonds requires significant energy [33] making AlN brittle and resistant to such plastic deformation. Mastro *et al* [29] showed that a critical AlN film thickness of around 300 nm exists

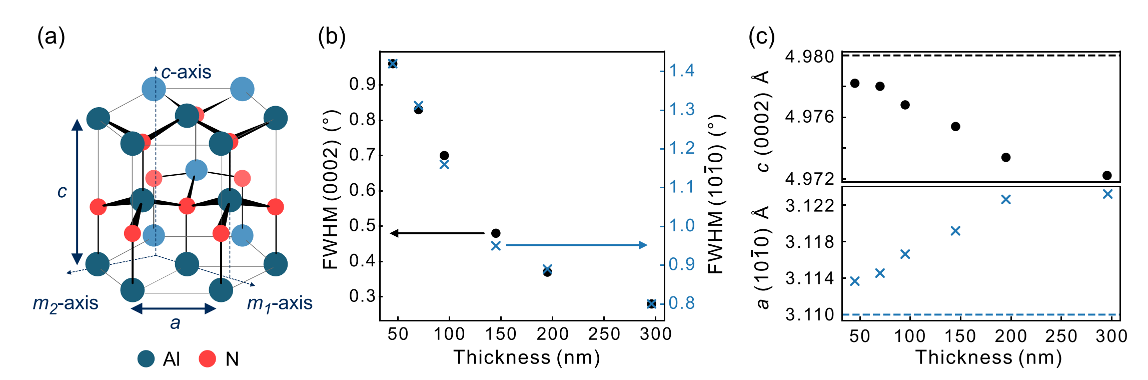

Figure 1. Crystal structure of AlN thin films. (a) Illustration of the wurtzite AlN crystal, where the m_1 and m_2 axes point along two mirror planes of the crystal. (b) HRXRD measurements: FWHM of (0002) and (10$\bar{1}$0) ω-scans as a function of AlN thickness. (c) Lattice constant: (0002) corresponds to the c-axis (top panel) and (10$\bar{1}$0) corresponds to the m-axis (bottom panel). Dashed lines are the single-crystal values.

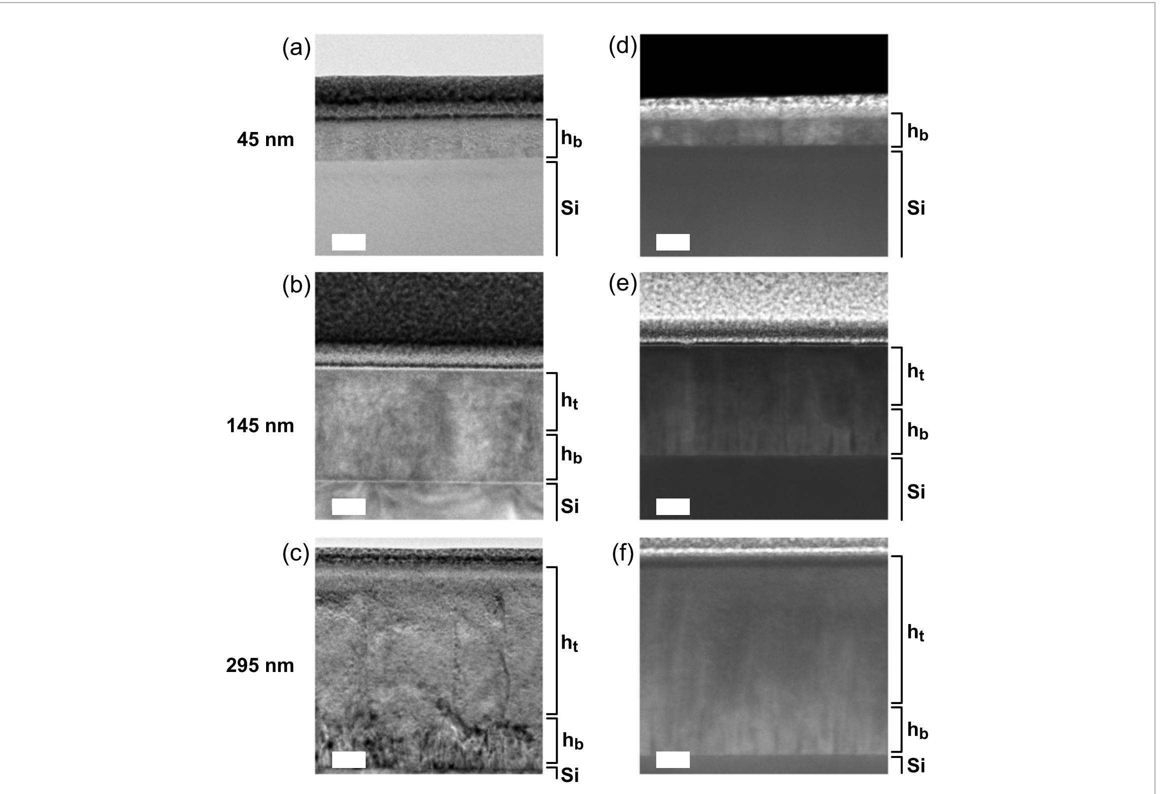

Figure 2. STEM and TEM imaging of AlN thin films. (a)–(c) STEM images (labeled by thickness determined through ellipsometry at the center of the wafer), (d)–(f) TEM images of AlN films on a Si (111) substrate. The scale bar is 50 nm.

beyond which the AlN film starts cracking at misfit dislocations. We observe that our 295 nm-thick AlN film exhibits cracks at the edge of the wafer, i.e. this film thickness appears to be the thickest to be usable for realizing AlN nanomechanical resonators.

2.2. Film morphology

To determine the thickness and the lateral variation of the AlN films, we perform spatially-resolved ellipsometry measurements across the wafer. For the nominally 295 nm-thick AlN film, we observe that the film thickness decreases to 280 nm at the edge of the 2 inch wafer. For all following analysis, we therefore use chips taken from the center of the wafer and refer to the AlN film thickness at the wafer's center.

We performed transmission electron microscopy (TEM) and scanning TEM (STEM) imaging to evaluate the microscopic quality of the MOVPE-grown AlN film. All of the III-nitrides have smaller interatomic spacing within their basal planes compared to (111) silicon as well as higher thermal expansion coefficients. These two properties result in an interface layer with a high density of misfit dislocations [34]. In the TEM images shown in figure 2 such a defect-rich layer [35] at the interface of the AlN film and the Si substrate is

Figure 3. 10×10 μm^2 AFM maps of AlN films. The crystal orientation (same for all scans) is indicated in the first map.

Table 1. Surface roughness of AlN thin films. RMS roughness of the AlN films over a 10×10 μm^2 scan window before and after fabrication of devices.

h (nm)	45	70	90	145	195
RMS as-grown (pm)	355 ± 32	270 ± 6	402 ± 83	348 ± 30	244 ± 37
RMS processed (pm)	–	–	521 ± 6	384 ± 6	408 ± 12

observed. From the change in morphology of the AlN films that are thicker than 100 nm (see figures 2(b),(c), (e) and (f)), we estimate that this defect-rich layer is about 70 nm. This motivates us to introduce a simple bilayer model, which we will use to model the properties of nanomechanical resonators. This model accounts for the crystal structure difference between two layers, but neglects the gradual transition of the AlN film's crystal structure from polycrystalline to single-crystal-like. The first region close to the substrate, denoted as h_{b}, consists of many dislocations and misoriented domains and is about 70 nm thick. Later, we fix the thickness of the defect-layer by fitting the bilayer model to measurements of fabricated cantilevers. The second region, denoted as h_{t}, is an AlN layer of high-crystal quality. Note that the emergence of a defect-rich layer in the epitaxial growth of AlN on Si (111) substrate is similar to epitaxially-grown SiC on a Si substrate [19].

2.3. Surface roughness

The surface roughness of the AlN layer is measured by atomic force microscopy (AFM) in tapping mode for a scan size of 10×10 μm^2 (see figure 3). For each AlN thickness the measurements are performed at several locations of the wafer and the average root-mean-square (RMS) surface roughness is determined (see table 1). A smooth surface is essential to obtain low optical and mechanical loss. When the films have RMS surface roughness well below 1 nm then the optical scattering loss is small and the film is excellent for photonic applications. A low surface roughness is also an indicator of a surface with few dangling bonds and defects and, as a result, a larger intrinsic mechanical quality factor [36]. We compare the surface roughness of unprocessed and processed AlN films of different thickness in table 1. We observe that the surface roughness of all AlN films is below 1 nm, even after fabrication of devices. However, the RMS is slightly higher in the latter case, which could be due to the etching steps in the fabrication process.

2.4. Piezoelectricity

AlN has three piezoelectric coefficients d_{31}, d_{15}, and d_{33}. Among them, the piezoelectric coefficient d_{33} is commonly used to quantify the piezoelectricity of AlN [21]. We use piezoresponse force microscopy (PFM) to determine the effective piezoelectric coefficient d_{33}^{eff} (see [21] for details of the measurement procedure performed with a commercial Bruker Dimension ICON AFM). PFM is based on the inverse piezoelectric effect. An AC modulation signal is applied to the surface of the AlN film through the PFM probe in contact mode. The deformation of the film induced by the electric field is detected by the PFM probe, see figure 4(a). The measurement results are effective piezoelectric values which are smaller than d_{33} due to the clamping constraint of the film through the substrate [37] and, potentially, the stress in the film [38]. Figure 4(b) shows that the effective piezoelectric coefficient increases with the thickness of AlN. This behavior can be explained by the improved crystal quality of thicker AlN films, which, thus, have larger polarized domains.

2.5. Residual stress

A method to assess the residual stress of the film is to perform Raman measurements [21]. Figure 5(a) shows Raman spectra for the AlN films. Between 600 to 680 1/cm we observe the two Raman-active phonon modes A_1 and E_2^{high} [39, 40], which both shift due to residual stress. We choose to use the clear and strong signal

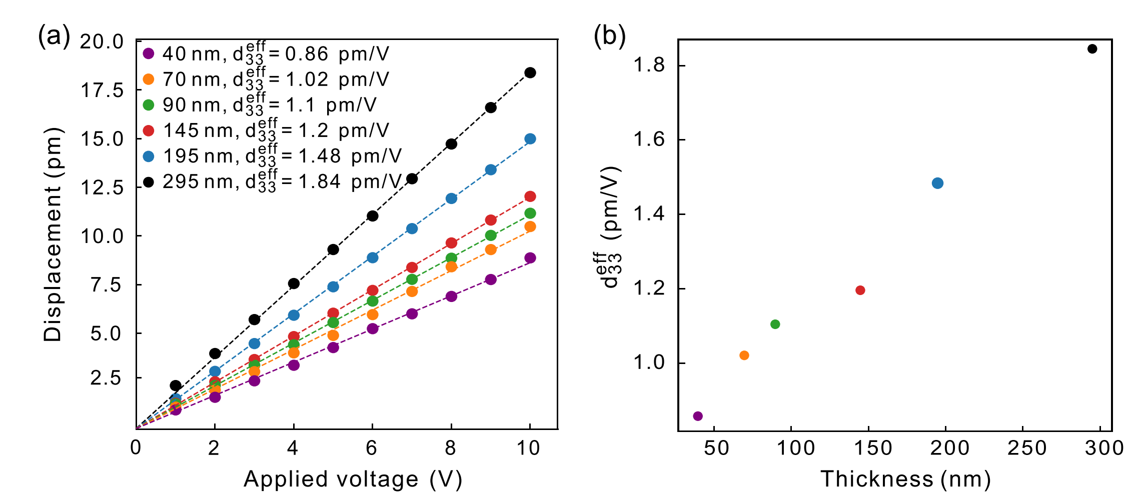

Figure 4. Piezoresponse force microscopy. (a) Piezoelectrically-induced displacement vs. applied voltage (dashed line is a linear fit). (b) Mean values and uncertainty of the effective piezoelectric coefficient vs. thickness of the AlN film. Note that the uncertainty is in most cases smaller than the point size.

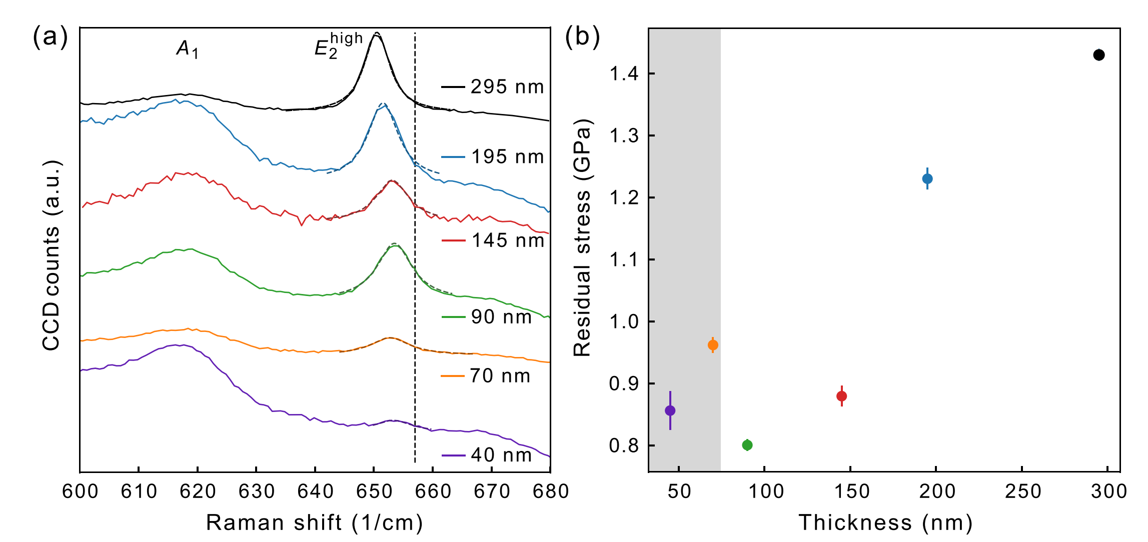

Figure 5. Raman measurements to determine residual stress. (a) Raman spectra of AlN thin films. The position of the E_2^{high} phonon mode is fitted. Dashed black line at 657 cm^{-1} is the single-crystal value. (b) Evaluated $\sigma_{residual}$ of the AlN film vs. thickness. The grey area marks the thickness of the defect-rich layer region.

given by mode E_2^{high} to infer the stress in the AlN layer (see also [41, 42]) as mode A_1 shows a broader peak and the analysis is more complex due to its polar nature. The shift of the E_2^{high} phonon mode in AlN, $\Delta\omega$, is related to the residual stress via [42]

$$\Delta\omega = 2\alpha_0\sigma_{residual}. \tag{1}$$

The conversion of $\Delta\omega$ to stress in the film depends on the deformation potential constant, α_0, which varies for each AlN thickness due to the presence of the defect-rich layer. To get an estimate of the residual stress in the AlN thin films, we use the bulk single-crystal value of AlN ($\alpha_0 = 2.2115$ cm^{-1}/GPa [43]). Figure 5(a) shows the Raman spectra and figure 5(b) the evaluated residual stress of the AlN thin films. We observe that $\sigma_{residual}$ monotonously increases with film thickness for films thicker than 90 nm with a maximal value of 1.4 GPa for the 295 nm-thick film. Thin films below 90 nm show a different behavior, which we attribute to the 70 nm-thick defect-rich layer, which is expected to have different elastic properties than the single-crystal case.

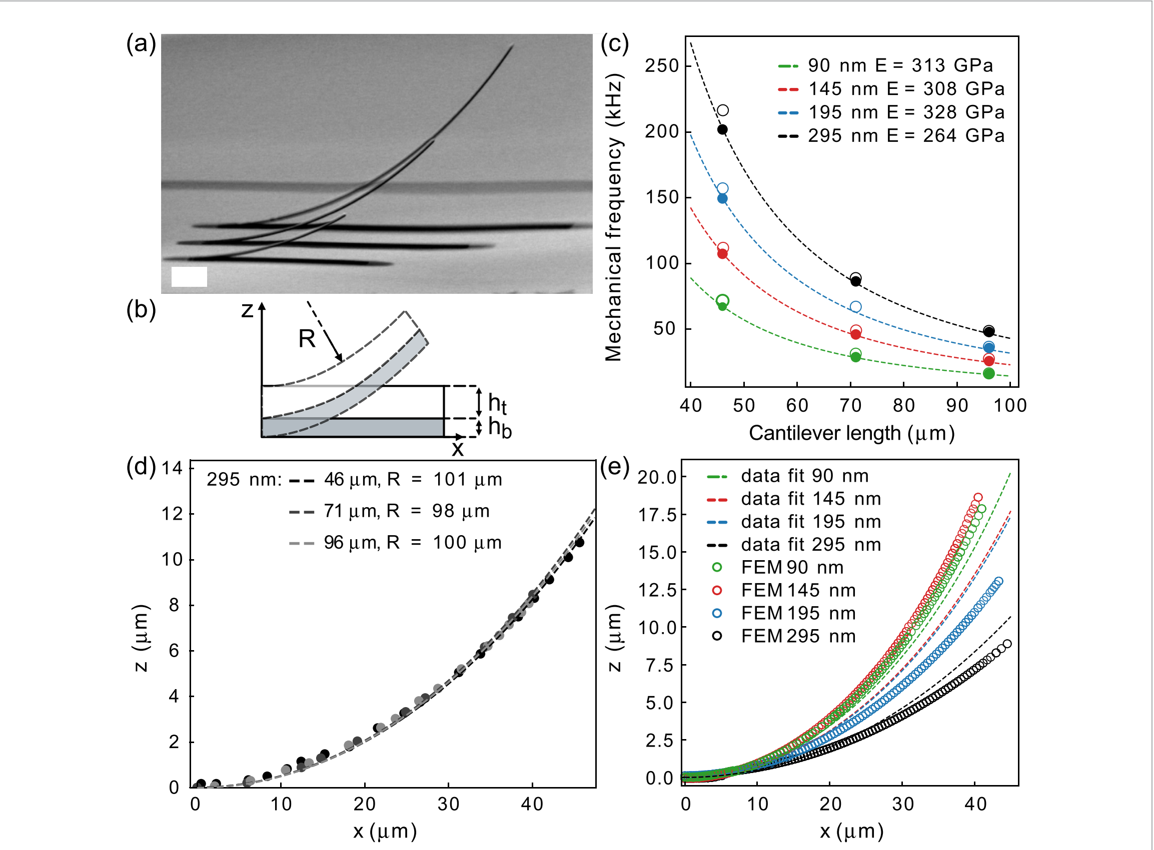

Figure 6. AlN cantilevers. (a) Tilted SEM image of 46 μm-, 71 μm-, and 96 μm-long cantilevers fabricated from 295 nm-thick AlN. The scale bar is 10 μm. (b) Sketch of the bilayer model. (c) Fundamental mechanical mode frequency for cantilevers of different length and thickness. The dashed line is a fit to equation (2), dots are the measured data, and empty circles are the FEM results using the bilayer model. (d) Confocal microscope data (dots) and fit (dashed lines) for 295 nm-thick AlN cantilevers of different length. (e) Bending of 46 μm-long cantilevers for 90 nm-, 145 nm-, 195 nm- and 295 nm-thick AlN films. The dashed lines are fits to confocal microscope data with the values from table 2 and open dots are FEM results using the bilayer model.

3. Cantilevers

We fabricated cantilevers of varying lengths L (46 μm, 71 μm, and 96 μm) to determine Young's modulus of the AlN thin films (details of the fabrication are found in appendix A.3). Figure 6(a) shows that the cantilevers bend upwards upon release. This bending can be explained by an inhomogenous strain in the AlN film, which originates from the movement of edge dislocations and their annihilation as the AlN layer becomes thicker. To model the observed bending, we use the bilayer model. We assume that the two layers of the bilayer model exhibit a difference in strain, ϵ_z (see figure 6(b)). For simplicity, we assume that Young's modulus is the same for both layers. We will use this model in all FEM simulations of the various nanomechanical resonators that we analyze (details see appendix A.4). Further, we measure the relevant properties of the fabricated nanomechancial resonators in a high vacuum chamber (7×10^{-6} mbar, if not stated otherwise) at room temperature using an optical interferometric position measurement setup [21].

3.1. Young's modulus

The mechanical frequencies of the modes of a cantilever are given as [44]

$$f_c = \frac{\lambda_n^2}{2\pi L^2}\sqrt{\frac{Eh^2}{12\rho}}, \tag{2}$$

where $\lambda_1 = 1.8751$ for the fundamental mode. This formula assumes that the AlN film is vertically uniform, i.e. that Young's modulus and the film's density ($\rho = 3255$ kg m^{-3}) is the same over the thickness of the cantilever. We will make this simplification here to extract an *effective* Young's modulus, E, for our AlN film. We determine that E is around 310 GPa for AlN films with thicknesses of 90 nm, 145 nm, and 195 nm (figure 6(c) and table 2), but only 264 GPa for the 295 nm-thick AlN film. Note that the latter value is in agreement with [21], which determined $E = 265 \pm 5$ GPa from measurements of higher-order modes of

Table 2. Residual stress and Young's modulus. The measured residual stress as determined from Raman measurements compared to the average residual stress of the bilayer model used in FEM simulations. The effective Young's modulus is determined from the fundamental mode frequency of cantilevers using equation (2). f_c^{meas} (f_c^{FEM}) and f_b^{meas} (f_b^{FEM}) are the measured (FEM simulated) fundamental frequency of 46 μm-long cantilevers and 200 μm-long beams, respectively.

	σ (GPa)		E (GPa)	$R(\mu\text{m})$	f_c (kHz)		f_b (MHz)	
h (nm)	measured	σ_{avg}	measured	measured	measured	FEM	measured	FEM
90	0.79	0.75	313	60.8 ± 0.5	67	71	0.97	1.02
145	0.88	1	308	67.9 ± 1.7	107	112	1.1	1.18
195	1.23	1.1	328	66.4 ± 0.8	149	158	1.3	1.25
295	1.4	1.2	264	100 ± 1.5	202	218	1.4	1.3

uniform beams. We suggest that the lower value of E that is only observed for the 295 nm-thick film could be the result of approaching the critical thickness of the AlN film in our high-temperature MOVPE growth.

3.2. Bilayer model

In a bilayer structure of layer thicknesses h_t and h_b, a strain difference ϵ_z between the layers creates a torque upon release. This torque results in bending of a cantilever with a radius of curvature R of [45]

$$\frac{1}{R} = \frac{6\epsilon_z (1+m)^2}{h\left[3(1+m)^2 + (1+m)(m^2+1/m)\right]} = \frac{6\epsilon_z h_t h_b}{h^3}, \tag{3}$$

where $m = h_t/h_b$.

Using a confocal microscope, we measure the bending curvature of 46 μm-, 71 μm-, and 96 μm-long cantilevers near the clamping points. We fit the data to a circle equation and observe that the bending radius is consistent for cantilevers of a given thickness, see figure 6(d). This result is expected from equation (3), as the radius of curvature depends solely on the strain difference and layer thicknesses, but not on the cantilever's length.

Figure 6(e) shows the bending of AlN cantilevers of various thickness. Overall, the bending radius increases with AlN film thickness (summarized in table 2). This is because with increasing thickness the contribution of the single-crystal layer to the entire thickness of the AlN film becomes larger, while the thickness of the defect-rich layer remains constant, thus, reducing the overall bending.

To replicate the bending in the FEM simulations, we model the bottom layer with $h_b = 72.5$ nm and a residual stress of $\sigma_{\text{residual,b}} = 0.6$ GPa, and the top layer with $h_t = h - h_b$ and residual stress of $\sigma_{\text{residual,t}} = 1.4$ GPa. The average residual stress, σ_{avg}, is then given as the weighted mean of the two layers, i.e. $\sigma_{\text{avg}} = (h_b\sigma_{\text{residual,b}} + h_t\sigma_{\text{residual,t}})/h$. This value is comparable to the residual stress determined from Raman measurements (see table 2). Figure 6(e) compares the cantilever bending obtained from FEM simulations to the measurements. In general, the overall bending behaviour is quite well captured by the FEM simulations. However, the 145 nm- and 195 nm-thick cantilevers bend similarly in the experiment, which is not captured in FEM. This slight discrepancy points to a limitation of the simple bilayer model, which neglects the gradual change in crystal structure that occurs during epitaxial growth.

4. Beams

The released stress (σ_{released}) and intrinsic quality factor (Q_{int}) of the AlN thin films can be determined from measurements of the eigenfrequencies of uniform beams [46]. To this end, we have fabricated beams of various lengths (75 μm to 200 μm) and in-plane orientation angles α (0° to 180°), see inset figure 7(a), as either quantity could be dependent on the orientation of the beam with respect to the crystallographic axes. This is different compared to nanomechanical resonators fabricated from isotropic, e.g. amorphous or polycrystalline, materials. Appendix A.3 shows images of fabricated beams.

4.1. Released stress

For a beam under tensile stress, σ_{released}, the fundamental mode frequency is given by [47]

$$f_b = \frac{1}{2L}\sqrt{\frac{\sigma_{\text{released}}}{\rho}}, \tag{4}$$

where L is the length of the beam. By measuring the fundamental mode's eigenfrequency of beams of various lengths (figure 7(a)), we determine the released stress through a fit of the data to equation (4). Figure 7(b) shows the dependence of the released stress on the orientation of the beam with respect to the crystal axes.

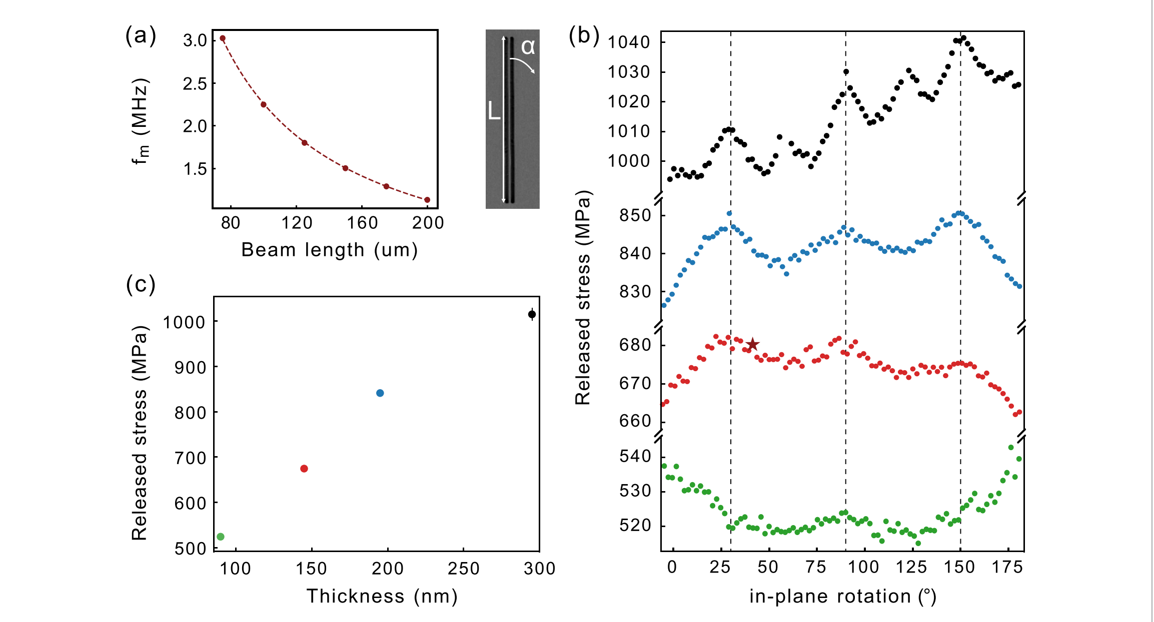

Figure 7. Released stress. (a) Fundamental mode frequency in dependence of beam length in 145 nm-thick AlN. The fit yields σ_{released} (star in panel (b)). Right: SEM image of a beam. (b) The dependence of σ_{released} on the beam's in-plane orientation. Dashed vertical lines indicate a 60 ° periodicity. (c) Averaged σ_{released}.

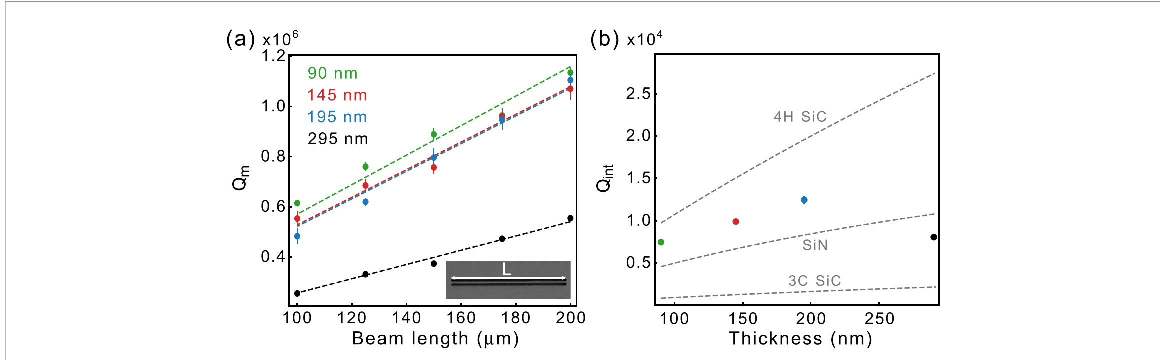

Figure 8. Intrinsic mechanical quality factor of AlN thin films. (a) Data and fit of Q_{m} for 90 nm-, 145 nm-, 195 nm- and 295 nm-thick AlN beams. The inset shows an SEM image of a 200 μm-long beam. (b) Calculated Q_{int} using the $\epsilon_{\text{released}}$ values from table 3. The dashed lines show the model of Q_{int} for SiN [48], 3 C SiC [19] and 4 H SiC [20].

We observe a 60° periodicity, as is expected from the wurtzite crystal structure of AlN [21]. For the 295 nm-thick AlN, the released stress is about 1 GPa, whereas for the 90 nm-thick film, the stress decreases to 520 MPa, see figure 7(c) and table 3. The measured released stress aligns well with the one calculated from the residual stress when accounting for its relaxation via the factor $(1-\nu)$ with the Poisson ratio $\nu = 0.28$.

4.2. Intrinsic quality factor

The quality factor of a strained, high-aspect-ratio mechanical resonator is enhanced by the dilution factor, D_Q, over the intrinsic quality factor, Q_{int} as [14]

$$Q_{\text{D}} = D_Q\, Q_{\text{int}}. \tag{5}$$

While Q_{int} is an intrinsic material property, inversely proportional to the delay between stress and strain, D_Q is determined by the mechanical mode's geometry and can be engineered. The dilution factor depends on the ratio of linear to nonlinear dynamic contributions to the elastic energy, which is specific to the mechanical mode shape [14, 21].

We determine Q_{int} by measuring the quality factor Q_{beam} (see figure 8(a)) of long, thin, strained uniform beams. Their quality factor is limited by dissipation dilution with $D_Q^{\text{beam}} = \left[(\pi\lambda)^2 + 2\lambda\right]^{-1}$ and the stress parameter $\lambda = \frac{h}{L}(12\epsilon_{\text{released}})^{-1/2}$ [13]. We use the linear relation $\epsilon_{\text{released}} = \sigma_{\text{released}}/E$ (see table 3 for the values of E) and the values of Q_{beam} to determine the intrinsic quality factor. Note that in general the relation between strain and stress is given by a tensor, for details see [21]. As we do not have experimental access to

Table 3. Mechanical properties of the MOVPE-grown AlN films on Si (111). Residual stress σ_{residual}, the stress after release σ_{released}, and the strain $\epsilon_{\text{released}} = \sigma_{\text{released}}/E$ with Young's modulus E. The intrinsic quality factor Q_{int} quantifies the intrinsic mechanical loss.

h (nm)	σ_{residual} (GPa)	σ_{released} (GPa)	E (GPa)	$\epsilon_{\text{released}}$	Q_{int}
90	0.79	0.52	313	0.0017	7.4×10^3
145	0.88	0.68	308	0.0022	9.8×10^3
195	1.23	0.83	328	0.0025	1.24×10^4
295	1.43	1	264	0.0035	8×10^3

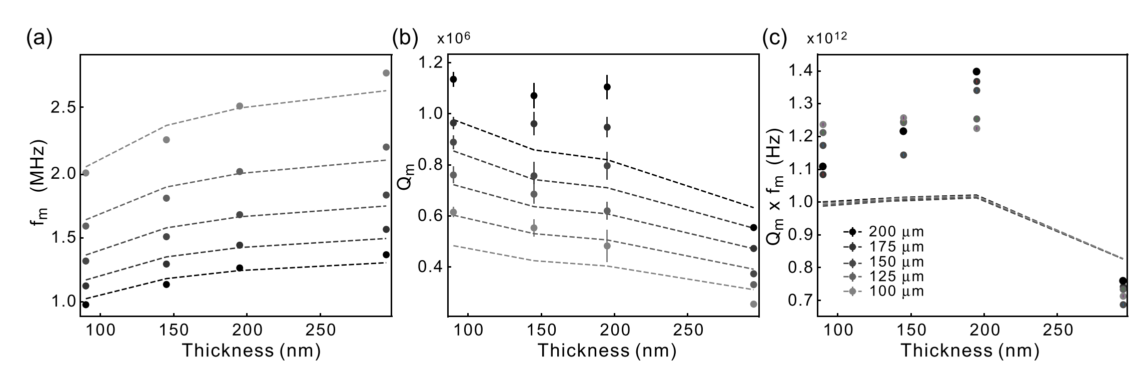

Figure 9. Mechanical eigenfrequency and quality factor of uniform beams fabricated from tensile-strained AlN thin films. (a) Mechanical frequency, f_{m}, (b) mechanical quality factor, Q_{m}, (c) $Q_{\text{m}} \times f_{\text{m}}$-product for various thicknesses and beam lengths. Dots are the measured data and dashed lines are the FEM simulation results using the bilayer model. Note that the FEM results for the $Q_{\text{m}} \times f_{\text{m}}$-product are independent of the beam's length as expected from the analytical scaling of f_{m} and Q_{m}.

the elastic constants for each AlN film thickness, but to an effective Young's modulus (see equation (2)), we make the simplifying assumption of a linear relation between stress and strain. The results are shown in figure 8(b). We observe that Q_{int} increases with AlN film thickness up to 195 nm-thick films with a value of $Q_{\text{int}} = 1.24 \cdot 10^4$. The thickest AlN film of 295 nm, however, shows a drastic decrease in Q_{int}. A possible reason could be that this film thickness is close to the critical thickness, which results in cracks at the edge of the wafer and, potentially, additional defects in the film, which would lower Q_{int}.

To understand the approximate linear thickness dependence of Q_{int} for AlN films thinner than 200 nm, we compare our results to a commonly-used model for Q_{int}. This model assumes that Q_{int} is determined by bulk loss, Q_{vol}^{-1}, and surface loss, Q_{s}^{-1}, as $Q_{\text{int}}^{-1} = Q_{\text{s}}^{-1} + Q_{\text{vol}}^{-1}$ [48]. For mechanical resonators with a large surface-to-volume ratio the intrinsic quality factor is predominantly limited by Q_{s}. Surface loss can originate from defects or impurities [48], dangling bonds [36], surface roughness [49], or surface oxidation [50, 51]. For example, for SiN nanomechanical resonators reference [48] determined $Q_{\text{vol}}^{\text{SiN}} = 2.8 \times 10^4$ and $Q_{\text{s}}^{\text{SiN}} = \beta_{\text{SiN}} \cdot h$ with $\beta_{\text{SiN}} = 6 \times 10^{10}$ 1/m, i.e. Q_{s} increases linearly with thickness (see figure 8(b)). We observe a similar behavior for AlN film thicknesses below 200 nm with a slope of 4.8×10^{10} 1/m. However, unlike SiN, the crystal properties of the AlN thin film change with thickness. We observe, for example, that Q_{int} of the 295 nm-thick AlN film is smaller than the one of the 195 nm-thick film. Thus, we cannot explain that abrupt change by a threshold behavior, which would be given by Q_{vol}. Overall, the Q_{int} that we determined for AlN thin films up to a film thickness of 200 nm is larger than the corresponding Q_{int} of SiN or epitaxially-grown 3 C SiC [19], but lower than the one of 4 H SiC [20] (figure 8(b)).

Let us also consider the $Q_{\text{m}} \times f_{\text{m}}$-product of the beams, which is a key figure of merit in quantum optomechanics. If $Q_{\text{m}} \times f_{\text{m}} > 6 \times 10^{12}$ Hz, then the beams would show at least one coherent oscillation at room temperature. The $Q_{\text{m}} \times f_{\text{m}}$-product is influenced by the film thickness. While thicker AlN films exhibit higher stress, and, thus, result in a larger mechanical frequency (figure 9(a)), their dilution factor decreases (figure 9(b)). Further, we observe a linear increase of Q_{int} with thickness only up to 200 nm-thick films. Consequently, there is an optimal film thickness that maximizes the $Q_{\text{m}} \times f_{\text{m}}$-product. Figure 9(c) shows the $Q_{\text{m}} \times f_{\text{m}}$-product of beams, where we obtain a maximum value of $1.4 \cdot 10^{12}$ Hz at a film thickness of 195 nm, similar to what we expect from FEM simulations using the experimentally determined material properties as input values.

There are several approaches to further improve the intrinsic quality factor, which would directly translate into a larger $Q_{\text{m}} \times f_{\text{m}}$-product. For instance, it can be increased by avoiding the defect-rich layer at the interface to the Si substrate as part of the nanomechanical resonator structure. Therefore, back-etching the 70 nm-thick, defect-rich layer should enhance Q_{int} [19]. Another method is wafer-bonding the AlN film to a different substrate and then thinning it down. This approach has been successfully demonstrated with

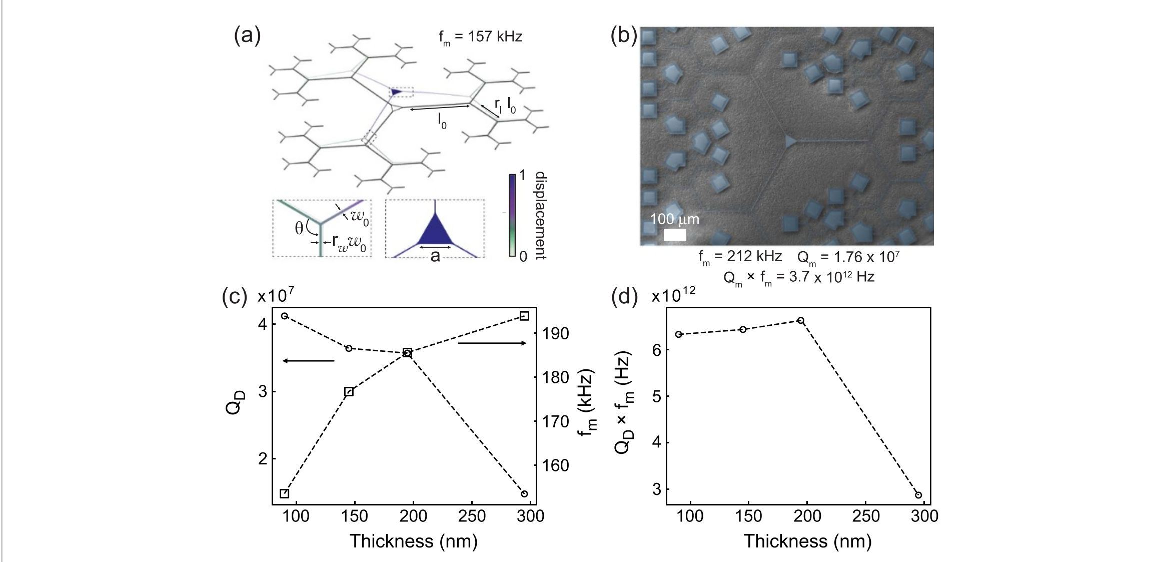

Figure 10. Hierarchically-clamped triangline resonators. (a) Schematic of a hierarchically-clamped triangline resonator showing the mechanical displacement of its fundamental mode. (b) False-colored SEM image of a fabricated device. (c) FEM simulated thickness dependence of Q_D and f_m for the triangline with an equivalent-length of 1.8 mm. (d) FEM simulated values of the $Q_D \times f_m$-product for the triangline, as a function of thickness.

4 H SiC [20], resulting in a high-quality thin film, but on the cost of reducing the residual stress of the layer. Released beams of wafer-bonded 4 H SiC exhibited a stress of 172 MPa only. Finally, it is possible to introduce a sacrificial layer below the AlN film. This alternation of the growth would relocate the defect-rich interface away from the thin device layer while preserving its stress [52].

5. High-Q_m nanomechanical triangline resonators

In the following, we demonstrate that the AlN thin films can also be used to realize a complex resonator geometry. To this end, we have chosen a hierarchically-clamped nanomechanical resonator [53], called triangline [21] (see figure 10(a)), which exploits dissipation dilution to increase Q_m. The triangline has three-fold symmetry and, thus, follows the Al-N bonds of the AlN crystal structure [21]. The resonator design features a central pad in the shape of an equilateral triangle with a side length of $a = 70\ \mu$m, suspended by beams of width $w_0 = 2.0\ \mu$m. At a length of $l_0 = 0.36$ mm, the string branches in two with an angle of $\theta = 120°$ between them. The width of these new branches is given by $w = r_w w_0$ with $r_w = 1/(2\cos(\theta/2)) = 1$, ensuring that the stress is preserved [53]. This branching process repeats $N = 6$ times, with the length of the branches being $l_0 \cdot r_l^i$ for the ith iteration, where $r_l = 0.61$. Finally, the last iteration of branches clamps the triangline to the substrate.

We use FEM simulations to predict Q_D and f_m for the triangline resonator. To this end, we employ the bilayer model with the material parameters that we have experimentally determined. The thickness-dependent values of Q_D and f_m (figure 10(b)), and the $Q_m \times f_m$-product (figure 10(c)) follow the same trend as was observed for the uniform beams (figure 9). The $Q_m \times f_m$-product of the triangline is expected to lie above $6 \cdot 10^{12}$ Hz when fabricating the triangline in AlN films that are thinner than 200 nm.

We chose to fabricate a triangline in the 90 nm-thick AlN film to demonstrate that the thinnest working AlN material can be used to fabricate such a complex resonator geometry. An SEM image of a fabricated device is shown in figure 10(b). We observe a fully released resonator structure. We measured a fundamental mode mechanical frequency of $f_m = 212$ kHz with a quality factor of $Q_m = 1.76 \times 10^7$ at a pressure of 4×10^{-8}, yielding a $Q_m \times f_m$-product of 3.7×10^{12} Hz, which is slightly lower than the one we expected from FEM simulations. In reference [21] we realized a triangline of similar length, but in 295 nm-thick AlN and measured a $Q_m \times f_m$-product of its fundamental mode of 2.5×10^{12} Hz. Hence, with the thinner 90 nm-thick AlN film, the $Q_m \times f_m$-product increased by a factor of 1.5, close to what we expect from FEM simulations (figure 10(c)).

6. Conclusion and outlook

We characterized piezoelectric tensile-strained AlN thin films with thicknesses ranging from 45 nm to 295 nm for high-Q_m nanomechanics. We identified a defect-rich region of about 70 nm thickness in the AlN

film that prevented the release of resonators from films thinner than 90 nm. We determined the highest intrinsic quality factor of $1.2 \cdot 10^4$ in the 195 nm-thick AlN film that showed a residual stress of 1.23 GPa. These values are comparable to other thin film materials used for high-Q_m nanomechanics exploiting dissipation dilution. We found that the $Q_m \times f_m$-product of AlN films thinner than 200 nm remained nearly constant, as their intrinsic quality factor and stress increased with film thickness, while their dilution factor decreased. Importantly, we showed that the crystalline AlN thin film can be used to realize a complex nanomechanical resonator geometry. To this end, we demonstrated a hierarchically-clamped and triangline-shaped nanomechanical resonator [21] in the 90 nm-thick AlN film. The fundamental mode of this resonator reached a $Q_m \times f_m$-product of 3.7×10^{12} Hz, which is 1.5 times larger than the best value achieved with a similar triangline in 295 nm-thick AlN [21].

Our results give clear insights on how to increase the $Q_m \times f_m$-product in tensile-strained AlN nanomechanics beyond 10^{13} Hz. The MOVPE-based growth of the AlN thin film should be altered such that the defect-rich AlN layer at the interface to the Si substrate is avoided via, e.g. introducing a sacrificial layer [52]. Furthermore, the thickness of the AlN layer shall be well below the critical thickness in MOVPE-based growth [29] such that the in-built tensile stress can be maximized. Finally, the growth can be adapted to include doped AlGaN layers [54] around the tensile-strained AlN film such that its piezoelectricity can be harnessed in optoelectromechanical quantum devices [15].

Data availability statement

Data underlying the results presented in this paper are available in the open-access Zenodo database: https://doi.org/10.5281/zenodo.13 890 720 [55].

Acknowledgment

This work was supported by the Knut and Alice Wallenberg (KAW) Foundation through a Wallenberg Academy Fellowship (W W), the KAW Project No. 2022.0090, and the Wallenberg Center for Quantum Technology (WACQT, A C), and the Swedish Research Council (VR Project No. 2019-04946). H P acknowledges funding by the European Union under the project MSCA-PF-2022-OCOMM. MOVPE of AlN on Si was performed at Otto-von-Guericke-University Magdeburg. The mechanical resonators were fabricated in the Myfab Nanofabrication Laboratory at Chalmers and analyzed in Chalmers Materials Analysis Laboratory.

Disclosures

Witlef Wieczorek is a shareholder in WACQT-IP AB.

Appendix. Methods

A.1. Growth

The AlN film was grown by metal–organic vapour-phase epitaxy (MOVPE, AIXTRON AIX 200/4 RF-S) on a 2 inch 500 μm-thick highly As-doped silicon (111) wafer. After a thin Al deposition, the growth of AlN was performed in two regimes. First 20 nm were grown at a low growth rate with a surface temperature of 1110 °C, 100 mbar, and a high V-III ratio of 2500. Then the main AlN layer was grown at a high growth rate at 70 mbar and a low V-III ratio of 25 with a surface temperature of 1120 °C. By varying the time of the main deposition, samples with different AlN thicknesses were produced.

A.2. Material characterization

A.2.1. XRD measurements

HRXRD measurements were performed to obtain information about the crystallographic structure and orientation of the AlN thin films. In an ω-scan the incident x-ray beam's angle to the selected lattice plane is varied, while the detector angle 2Θ is fixed. Such scan can be performed in a grazing incidence in-plane diffraction (GIID) setup. The measurement in such a configuration is shown in figure A1(a). Grazing incidence means that the incident x-ray beam comes in at a very shallow angle (close to parallel) to the surface and the measured diffraction is collected in the plane of the sample surface. This scan gives information on in-plane orientation disorder of the crystallites (c-axis twist).

Another useful measurement of the c-axis disorder (tilt) can be performed by a slight variation of the incident ω angle when the detector angle is fixed to the symmetric lattice plane (0002). The measurement is shown in figure A1(b). When the ratio between the maximum of the ω-scan ($\omega = \Theta$) and detector is kept

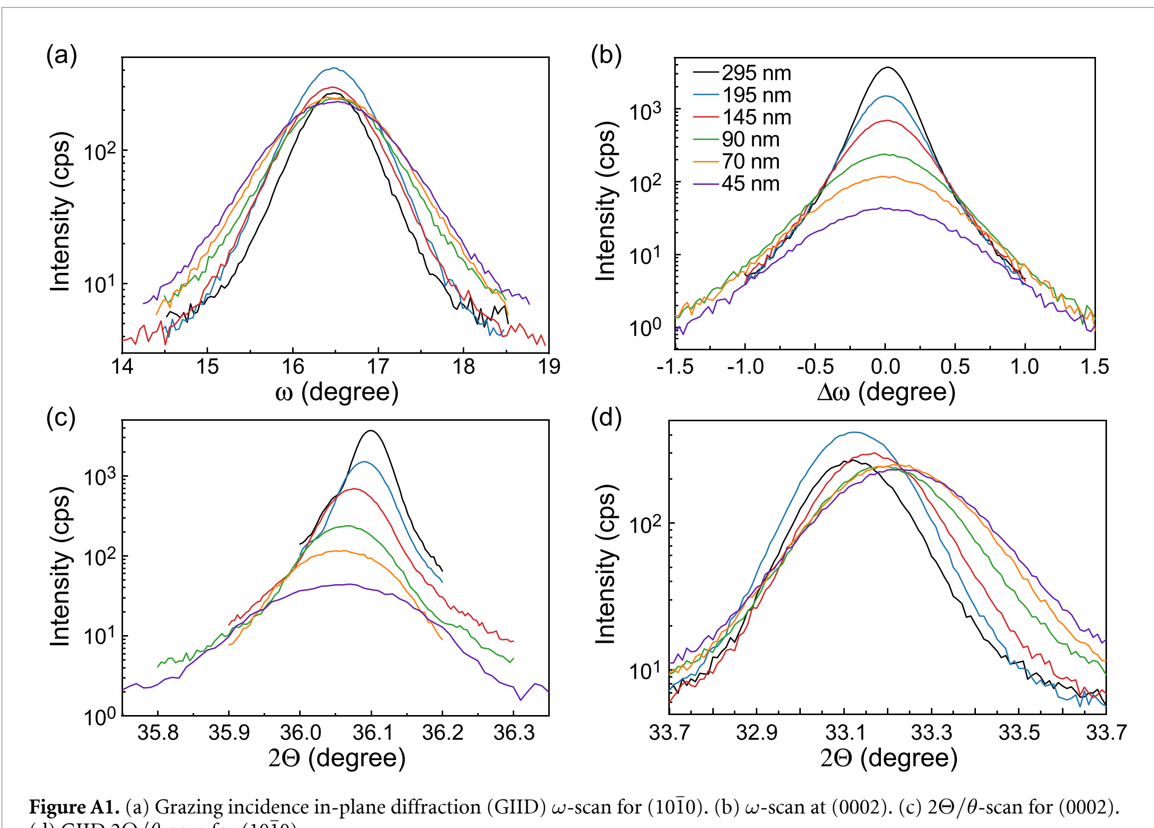

Figure A1. (a) Grazing incidence in-plane diffraction (GIID) ω-scan for $(10\bar{1}0)$. (b) ω-scan at (0002). (c) $2\Theta/\theta$-scan for (0002). (d) GIID $2\Theta/\theta$-scan for $(10\bar{1}0)$.

constant during the scan ($2\Theta/\theta$-scan), the lattice parameters are determined (i.e. the c value), see the measurement in figure A1(c). To examine the in-plane lattice parameter (i.e. a), a $2\Theta/\theta$-scan is performed in GIID setting (on $10\bar{1}0$), see the measurement in figure A1(d).

A.2.2. Raman measurements

Raman scattering is measured using a confocal Raman microscope at room temperature with a 532 nm laser for excitation. The laser beam is focused by an objective lens with a magnification of 100× and a numerical aperture of 0.9, leading to an optical spot size of about 300 nm. We verified that the Raman signal is power independent and, thus, unaffected by a potential heating of the device.

A.3. Fabrication process

The fabrication of nanomechanical resonators begins by sputtering a 50 nm SiO_2 hard mask. Subsequently, we define the pattern of the mechanical resonator in electron-beam resist (UV-60). Then we transfer the pattern into the hard mask and AlN film in consequent ICP/RIE etching steps with CF_4/CHF_3 and Cl_2/Ar mixtures, respectively. We strip the photoresist with NMP (Remover 1165), and the sample is cleaned with one minute HF etching. When the AlN film is suspended by etching Si with XeF_2, 45 nm- and 70 nm-thick AlN peeled off the substrate, see figure A2(a). This indicates that such films mostly consist of a defect-rich layer. Instead, AlN films with a thickness above 90 nm can be successfully suspended, figure A2(b). Note that we observed that the 90 nm-thick AlN film is grainy after XeF_2 etching (highest RMS roughness of all films, see table 1), while thicker films are not (see figure A3).

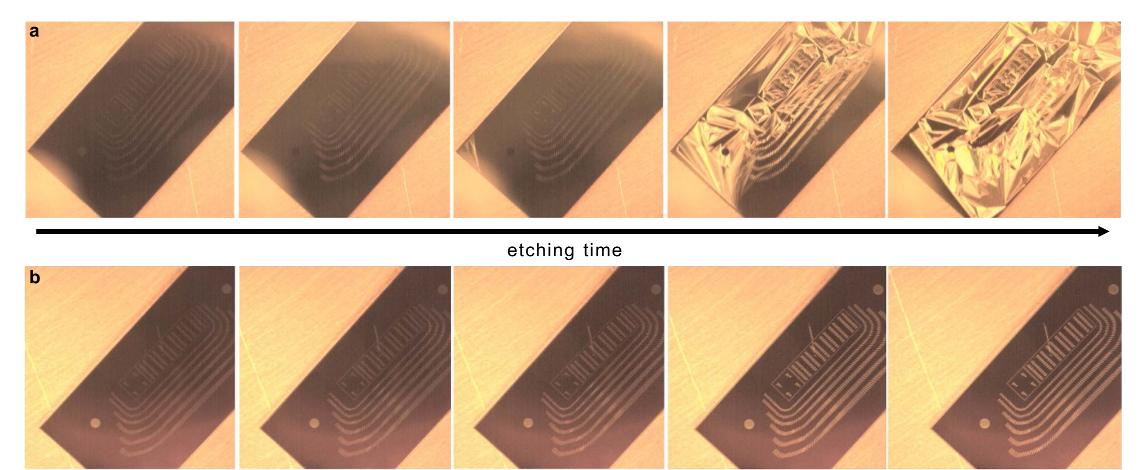

Figure A2. Time-dependent release process of AlN thin films. Temporal snapshots of the XeF_2 etching process of 5 mm × 10 mm chips for (a) 70 nm-thick AlN, and (b) 195 nm-thick AlN.

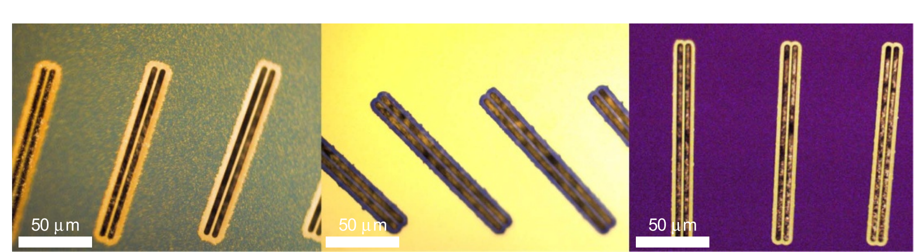

Figure A3. Optical microscope images of uniform beams fabricated from 90 nm-, 145 nm- and 195 nm-thick AlN.

A.4. Finite element simulations

We use the solid mechanics interface of COMSOL Multiphysics for FEM simulations and show examples of simulated devices in figure A4. Details of the simulations can be found in [21]. Here, we assume an isotropic material in our simulations as we use the experimentally determined values, among them Young's modulus, Q_{int}, and stress (see table 3). Additionally, we use as parameters an AlN density of 3255 kg m^{-3} and Poisson's ratio of 0.28.

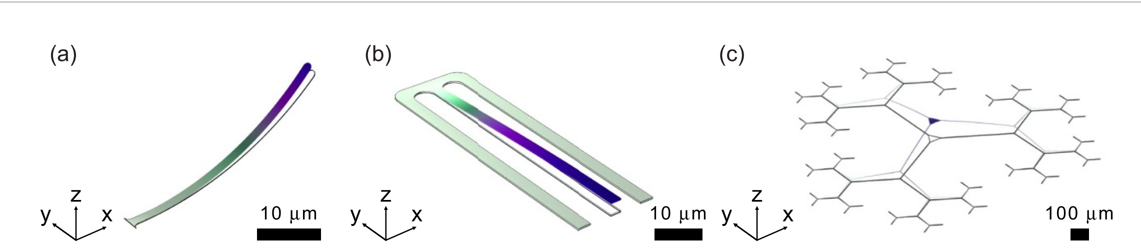

Figure A4. FEM simulations of the mechanical displacement for the fundamental out-of-plane oscillation mode of (a) cantilever, (b) beam (mirror symmetry is applied), and (c) triangline.

ORCID iDs

Joachim Ciers https://orcid.org/0000-0002-2753-5094
Hannes Pfeifer https://orcid.org/0000-0002-1713-6102
Witlef Wieczorek https://orcid.org/0000-0003-1847-053X

References

[1] Ekinci K and Roukes M 2005 *Rev. Sci. Instrum.* **76** 061101
[2] Chaste J, Eichler A, Moser J, Ceballos G, Rurali R and Bachtold A 2012 *Nat. Nanotechnol.* **7** 301–4
[3] Bachtold A, Moser J and Dykman M 2022 *Rev. Mod. Phys.* **94** 045005
[4] Eichler A 2022 *Mater. Quantum Technol.* **2** 043001
[5] Aspelmeyer M, Kippenberg T J and Marquardt F 2014 *Rev. Mod. Phys.* **86** 1391–452
[6] Barzanjeh S, Xuereb A, Gröblacher S, Paternostro M, Regal C A and Weig E M 2022 *Nat. Phys.* **18** 15–24
[7] Engelsen N J, Beccari A and Kippenberg T J 2024 *Nat. Nanotechnol.* **19** 725
[8] Beccari A, Visani D A, Fedorov S A, Bereyhi M J, Boureau V, Engelsen N J and Kippenberg T J 2022 *Nat. Phys.* **18** 436–41
[9] Cupertino A, Shin D, Guo L, Steeneken P G, Bessa M A and Norte R A 2024 *Nat. Commun.* **15** 4255
[10] Ren H, Matheny M H, MacCabe G S, Luo J, Pfeifer H, Mirhosseini M and Painter O 2020 *Nat. Commun.* **11** 3373
[11] Dania L, Bykov D S, Goschin F, Teller M, Kassid A and Northup T E 2024 *Phys. Rev. Lett.* **132** 133602
[12] Gonzfilez G I and Saulson P R 1994 *J. Acoust. Soc. Am.* **96** 207–12
[13] Schmid S, Jensen K, Nielsen K and Boisen A 2011 *Phys. Rev.* B **84** 165307
[14] Fedorov S A, Engelsen N J, Ghadimi A H, Bereyhi M J, Schilling R, Wilson D J and Kippenberg T J 2019 *Phys. Rev.* B **99** 054107
[15] Midolo L, Schliesser A and Fiore A 2018 *Nat. Nanotechnol.* **13** 11–18
[16] Cole G D *et al* 2014 *Appl. Phys. Lett.* **104** 201908
[17] Bückle M, Hauber V C, Cole G D, Gärtner C, Zeimer U, Grenzer J and Weig E M 2018 *Appl. Phys. Lett.* **113** 201903
[18] Manjeshwar S K, Ciers A, Hellman F, Blasing J, Strittmatter A and Wieczorek W 2023 *Nano Lett.* **23** 5076–82
[19] Romero E, Valenzuela V M, Kermany A R, Sementilli L, Iacopi F and Bowen W P 2020 *Phys. Rev. Appl.* **13** 044007
[20] Sementilli L, Lukin D M, Lee H, Romero E, Vučković J and Bowen W P 2024 arXiv:2404.13893
[21] Ciers A, Jung A, Ciers J, Nindito L R, Pfeifer H, Dadgar A, Strittmatter A and Wieczorek W 2024 *Adv. Mater.* **36** 2403155
[22] Sinha N, Wabiszewski G E, Mahameed R, Felmetsger V V, Tanner S M, Carpick R W and Piazza G 2009 *Appl. Phys. Lett.* **95** 053106
[23] Tsubouchi K, Sugai K and Mikoshiba N 1981 Aln material constants evaluation and saw properties on AlN/Al_2O_3 and AlN/Si *1981 Ultrasonics Symp.* (IEEE) pp 375–80
[24] Villanueva L G, Karabalin R B, Matheny M H, Kenig E, Cross M C and Roukes M L 2011 *Nano Lett.* **11** 5054–9
[25] Piazza G, Stephanou P J and Pisano A P 2007 *J. Microelectromech. Syst.* **16** 319–28
[26] Ivaldi P, Abergel J, Matheny M, Villanueva L, Karabalin R, Roukes M, Andreucci P, Hentz S and Defaÿ E 2011 *J. Micromech. Microeng.* **21** 085023
[27] O'Connell A D *et al* 2010 *Nature* **464** 697–703
[28] Li T, Mastro M and Dadgar A 2010 *III–V Compound Semiconductors: Integration With Silicon-Based Microelectronics* (CRC press)
[29] Mastro M, Eddy J C Gaskill D, Bassim N, Casey J, Rosenberg A, Holm R, Henry R and Twigg M 2006 *J. Cryst. Growth* **287** 610–4
[30] Schuster M, Gervais P, Jobst B, Hösler W, Averbeck R, Riechert H, Iberl A and Stömmer R 1999 *J. Phys. D: Appl. Phys.* **32** A56
[31] Nix W and Clemens B 1999 *J. Mater. Res.* **14** 3467
[32] Marchand H *et al* 1999 *Mater. Res. Soc. Internet J. Nitride Semicond. Res.* **4** e2
[33] Jin R, Liu J, Zhang J and Yang H 2004 *J. Cryst. Growth* **268** 35
[34] Radtke G, Couillard M, Botton G, Zhu D and Humphreys C 2012 *Appl. Phys. Lett.* **100** 011910
[35] Mante N, Rennesson S, Frayssinet E, Largeau L, Semond F, Rouvière J, Feuillet G and Vennéguès P 2018 *J. Appl. Phys.* **123** 124215
[36] Mohanty P, Harrington D, Ekinci K, Yang Y, Murphy M and Roukes M 2002 *Phys. Rev.* B **66** 085416
[37] Kim I-D, Avrahami Y, Tuller H L, Park Y-B, Dicken M J and Atwater H A 2005 *Appl. Phys. Lett.* **86** 192907
[38] Berfield T A, Ong R J, Payne D A and Sottos N R 2007 *J. Appl. Phys.* **101** 024102
[39] Perlin P, Polian A and Suski T 1993 *Phys. Rev.* B **47** 2874
[40] Kazan M, Zgheib C, Moussaed E and Masri P 2006 *Diam. Relat. Mater.* **15** 1169–74
[41] Placidi M, Moreno J, Godignon P, Mestres N, Frayssinet E, Semond F and Serre C 2009 *Sens. Actuators* A **150** 64–68
[42] Callsen G *et al* 2014 *Phys. Rev.* B **90** 205206
[43] Dai Y, Li S, Sun Q, Peng Q, Gui C, Zhou Y and Liu S 2016 *J. Cryst. Growth* **435** 76–83
[44] Schmid S, Villanueva L G and Roukes M L 2016 *Fundamentals of Nanomechanical Resonators* vol 49 (Springer)
[45] Timoshenko S 1925 *JOSA* **11** 233–55
[46] Unterreithmeier Q P, Faust T and Kotthaus J P 2010 *Phys. Rev. Lett.* **105** 027205
[47] Klaß Y S, Doster J, Bückle M, Braive R and Weig E M 2022 *Appl. Phys. Lett.* **121** 2834205
[48] Villanueva L G and Schmid S 2014 *Phys. Rev. Lett.* **113** 227201
[49] Huang X, Feng X, Zorman C, Mehregany M and Roukes M 2005 *New J. Phys.* **7** 247
[50] Tao Y, Navaretti P, Hauert R, Grob U, Poggio M and Degen C L 2015 *Nanotechnology* **26** 465501
[51] Luhmann N, Jachimowicz A, Schalko J, Sadeghi P, Sauer M, Foelske-Schmitz A and Schmid S 2017 *Appl. Phys. Lett.* **111** 063103
[52] Kini Manjeshwar S, Elkhouly K, Fitzgerald J M, Ekman M, Zhang Y, Zhang F, Wang S M, Tassin P and Wieczorek W 2020 *Appl. Phys. Lett.* **116** 264001
[53] Bereyhi M J, Beccari A, Groth R, Fedorov S A, Arabmoheghi A, Kippenberg T J and Engelsen N J 2022 *Nat. Commun.* **13** 3097
[54] Ponce F A 2017 *Microstructure and Polarization Properties of III-Nitride Semiconductors* (CRC Press)
[55] Ciers A, Jung A, Ciers J, Nindito L R, Pfeifer H, Dadgar A, Bläsing J, Strittmatter A and Wieczorek W 2024 Thickness dependence of the mechanical properties of piezoelectric high-qm nanomechanical resonators made from aluminium nitride *zenodo* (available at: https://doi.org/10.5281/zenodo.13890720)